

Hypersonic properties of nematic and smectic polymer liquid crystals

J. K. Krüger, L. Peët, R. Siems, and H.-G. Unruh

Fachbereich Physik, Universität des Saarlandes, D-6600, Saarbrücken, Federal Republic of Germany

M. Eich, O. Herrmann-Schönherr, and J. H. Wendorff

Deutsches Kunststoff-Institut, Schlossgartenstrasse 6R, D-6100 Darmstadt, Federal Republic of Germany

(Received 4 August 1987)

We have investigated the elastic and the optical properties of nematic and smectic side chain polymer liquid crystals at hypersonic frequencies. In contrast to classical liquid crystals, the polymer materials show a significant coupling between the static order parameter and the square of the elastic strain ϵ_3 . The inverse shear stiffness constants do not diverge. All elastic constants behave continuously at the nematic-isotropic transition (T_{ni}). From certain optoacoustic properties and the refractive index functions, it follows that order-parameter fluctuations play no role at T_{ni} , but that the glass transition dominates the dynamic elastic properties at hypersonic frequencies.

I. INTRODUCTION

Although classical liquid crystals of low molecular weight (CLC's) show significant optical anisotropies^{1(a)–1(c)} only small elastic anisotropies are observed within the monodomain state.² This holds true even at hypersonic frequencies^{3,4} where the shear stiffness constants may become significant.⁵ This means that CLC's show only a very weak coupling between the static order parameter^{1(b),1(c)} and the classical elastic strain tensor components ϵ_{ij} .

On the other hand, oligomer single crystals with layer structure (e.g., paraffin single crystals) have moderate elastic anisotropies while the molecular layers themselves possess a large anisotropy $(c_{33} - c_{11})/c_{11} \approx 20$.^{6,7} In certain perfluoro-alkanes with hexagonal symmetry the anisotropy of the bulk material may even become strongly negative.⁸ The significant reduction of the stiffness constant c_{33} for longitudinal wave propagation along the molecular chain axis of these layer crystals is attributed to the small interlayer stiffness.^{6,7} Elastic anisotropies of nematic and smectic polymer side chain liquid crystals (PLC's) are thus expected to be small or even negative.

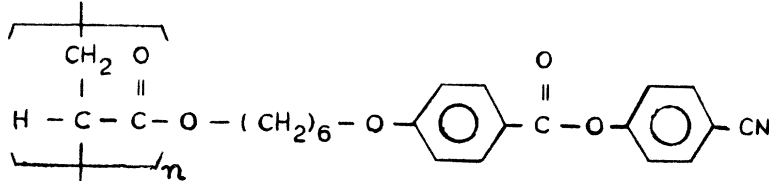
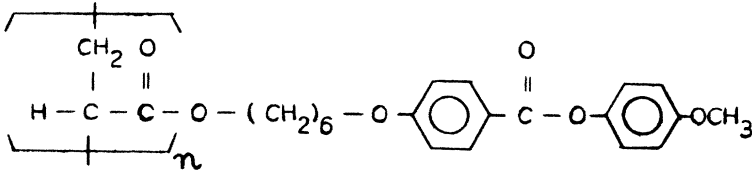
In nematic CLC's the anisotropy of the sound velocity of quasilongitudinal polarized phonons is typically of the order 10^{-2} with a maximum along the optical axis.² No acoustic attenuation anomalies are observed at the nematic-isotropic transition (T_{ni}) at hypersonic frequencies. Brillouin spectroscopic investigations of a PLC exist only for the smectic and nematic state of one polydomain sample.⁹ Concerning the elastic anisotropy of monodomain PLC's only preliminary data exist^{10(b)} which indicates an unexpectedly large elastic anisotropy with a maximum along the optical axis. However, this

sample contained oriented chromophore molecules. It could therefore not be excluded that part of the anisotropy was due to the influence of angle-dependent local heating of the sample.¹¹

Neutron scattering experiments^{12,13} show that the polymer main chains have a preference to be oriented orthogonal to the optical axis. The ratio of the mean dimensions of the chain molecules perpendicular and parallel to the director was found to be about 1.1 in the nematic and about 4 in the smectic-*A* phase. The conclusion was that the chain backbone is predominantly confined to the smectic layers.^{13,14} From these experiments the maximum of the sound velocity of longitudinal polarized phonons is then expected in these directions rather than along the optical axis.

In this paper we present Brillouin scattering results on the speed and polarization of sound waves in monodomain samples of the nematic and of the smectic-*A* polymers A and B, respectively, given in Table I. The polydispersity of the polymer molecules of both samples was $\bar{M}_w/\bar{M}_n \approx (2 \pm 0.1)$. For sample A the complete elastic stiffness tensor $\mathbf{c} = \{c_{ij}\}$ could be determined at room temperature in the frame of pure elasticity theory. Because of the reduced optical quality of sample B compared with that of sample A, the stiffness coefficient c_{66} of the former could not be measured yet. For sample A the temperature dependence of \mathbf{c} could be determined up to the isotropic phase. By comparing the refractive index functions $n_i(T)$ ($i=1,3$) with the optoacoustic D_i^{90R} functions [see Sec. III and Refs. 10(a) and 10(b)] the influence of relaxation processes in the vicinity of the nematic-isotropic phase transition will be discussed. It will be shown that these relaxation processes are not connected to the order-parameter fluctuations at T_{ni} but can be attributed to the dynamic glass transition.

TABLE I. Chemical formulas and transition temperatures (from DSC) of samples A and B.

sample	A
	
	$T_g = 295 \text{ K}, \quad T_{ni} = 378 \text{ K}$
	sample B
	
	$T_{gSA} = 300 \text{ K}, \quad T_{SA_{ni}} = 357 \text{ K}, \quad T_{ni} = 378 \text{ K}$

II. EXPERIMENTAL

Thin filmlike samples of thickness $d \sim 30 \mu\text{m}$ have been prepared using glass slides as support for the films. To prepare thin homogeneously aligned monodomain samples the surfaces of the glass slides were coated with a polyimide (Merck, Liquicoat PI) and rubbed along an arbitrary direction within the film plane which defines the director. The transition temperatures obtained for both samples from differential scanning calorimetry (DSC) measurements (heating rate: 10 K/min) are given in Table I.

For the interpretation of the elastic stiffness data we used an orthogonal reference frame with the x_3 axis parallel to the director and the x_2 axis orthogonal to the film plane. The monodomain samples had fiber symmetry. This was confirmed by measurements of the birefringence and is consistent with the elastic behavior (see Sec. III). The calculation of the stiffness coefficients c_{ij} (Voigt notation) was done using similar densities as obtained for acrylate side chain polymers with an identical chemical structure of the side chain:¹⁵ $\rho_A(300 \text{ K}) = \rho_B(300 \text{ K}) = 1100 \text{ kg/m}^3$ for samples A and B, respectively. Since the volume expansion coefficient of sample A is not yet known, we neglected the temperature dependence of ρ_A in our calculations of the elastic stiffness coefficients. This is justified because the influence of the volume expansion coefficients on the elastic constants is expected to be small compared to the observed elastic anomalies [$\alpha_n \approx \alpha_i \approx 5 \times 10^{-4} \text{ K}^{-1}$ (Refs. 15 and 16)].

The Brillouin measurements were made with a high-

performance Brillouin spectrometer using an argon-ion-laser at the vacuum wavelength $\lambda_0 = 514.5 \text{ nm}$. The characteristics of this spectrometer were discussed elsewhere.¹⁷ Figure 1 shows schematically the spectrometer setup which was used to obtain different realizations of the 90A- and 90R-scattering geometries^{10(b),18,19} described below. Using the shutters SH indicated in Fig. 1 we could discriminate between these two types of scattering geometries. Furthermore, the sample SA could be rotated in a defined way around x_2 (Fig. 1). The optical polarization conditions could be chosen using a Faraday ro-

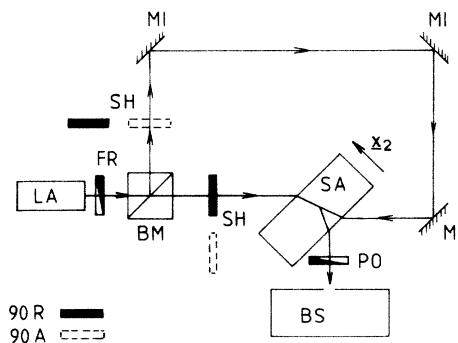


FIG. 1. Brillouin setup for a simultaneous measurement of different phonon modes. LA, argon ion laser; BM, beam splitter; FR, Faraday rotator; SH, shutters; SA, sample; MI, mirrors; PO, polarizer; BS, Brillouin spectrometer; x_2 , unit wave vector along the x_2 axis of the sample coordinate system. The 90A and 90R methods are explained in the text and in Fig. 2.

tator FR and a polarizer PO (Fig. 1). All these functions were computer controlled.

The principles of the 90A- and 90R-scattering geometries are shown in Figs. 2(a) and 2(b), respectively. The 90A method requires some comments. (i) A sound velocity polar plot (see, e.g., Figs. 4 and 5, curves I and II) can easily be obtained for sound wave propagation in the (x_1, x_3) plane of the sample by simply rotating it around x_2 [Fig. 2(a)]. (ii) Using proper optical polarization conditions, the involved acoustic wavelength $\Lambda^{90A} = \lambda_0 / \sqrt{2}$ does not depend on the optical properties of the sample. The 90R-scattering geometry is the only simple method for determining the elastic stiffness coefficient c_{66} of a thin film (c_{66} is not obtainable from 90A measurements).^{10(b),20} Presuming fiber symmetry of the LC films the 90A- and the 90R-scattering geometry can be used to determine the optoacoustic D_i^{90R} functions described in Sec. III. These functions provide a sensitive measure for the presence of hypersonic dispersion or deliver, in the absence of dispersion, directly the main refractive indices n_i ($i=1,3$). For sample A such measurements were performed as a function of temperature up to the isotropic state. For sample B such measurements are postponed until samples of better optical quality are available.

To avoid heating or burning of the sample, the effective laser power within the scattering volume was kept below 20 mW. The smallness of the scattering volume, together with this small illumination power, led to a rather low scattering intensity. Because of the resulting limited quality of the Brillouin spectra we abstain from a discussion of the hypersonic attenuation behavior. Excessive hypersonic attenuation can, however, be excluded, even in the vicinity of the nematic-isotropic transition temperature T_{ni} . Figure 3 shows a Brillouin spectrum for the phonon wave vector \mathbf{q} oriented within the (x_1, x_3) plane with an angle $\Phi \approx 45^\circ$ between \mathbf{q} and the x_3 axis. The full line in the spectrum is only a guide line. The intensity of the Rayleigh line R was reduced by a factor of 10^3 by means of a Pockels-cell as light modulator.¹⁸ The temperature dependent main refractive indices $n_1 = n_2$ and n_3 of sample A were determined with a prism method.

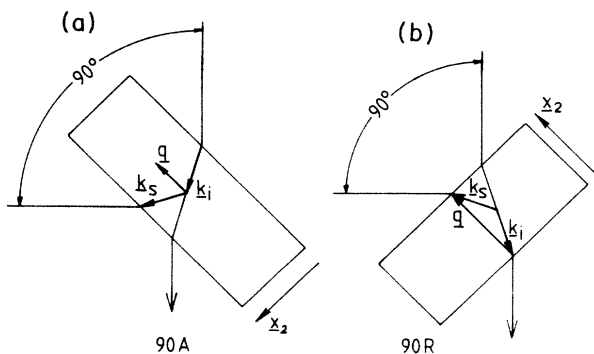


FIG. 2. Characteristics of the 90A- and 90R-scattering geometry. Outer scattering angle = 90° ; \mathbf{k}_i , wave vector of the incident laser beam; \mathbf{k}_s , wave vector of the scattered light; \mathbf{q} , phonon wave vector; x_2 , unit wave vector along the x_2 axis of the sample coordinate system.

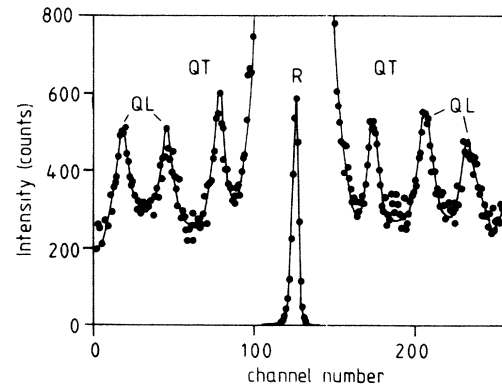


FIG. 3. Brillouin spectrum of sample A. Phonon wave vector \mathbf{q} oriented in the (x_1, x_3) plane $\Phi = \angle(\mathbf{q}, x_3) = 45^\circ$. QL (QT), Brillouin lines of quasilongitudinal (quasitransverse) phonons; R, Rayleigh line.

III. RESULTS AND DISCUSSION

The 90A-scattering geometry was used to determine sound velocity polar plots for the A and the B sample at room temperature by rotating the phonon wave vector \mathbf{q} within the (x_1, x_3) plane. Within the limits of error the influence of birefringence on the sound velocity results can be neglected.^{10(b)} Figures 4 and 5 show the measured data points for the quasilongitudinal (curve I) and quasitransverse (curve II) sound waves. Curve III in Fig. 4 represents the velocity of the pure shear mode. It was constructed from data points on the x_1 and the x_3 axes. The data point on the x_3 axis was obtained from 90A

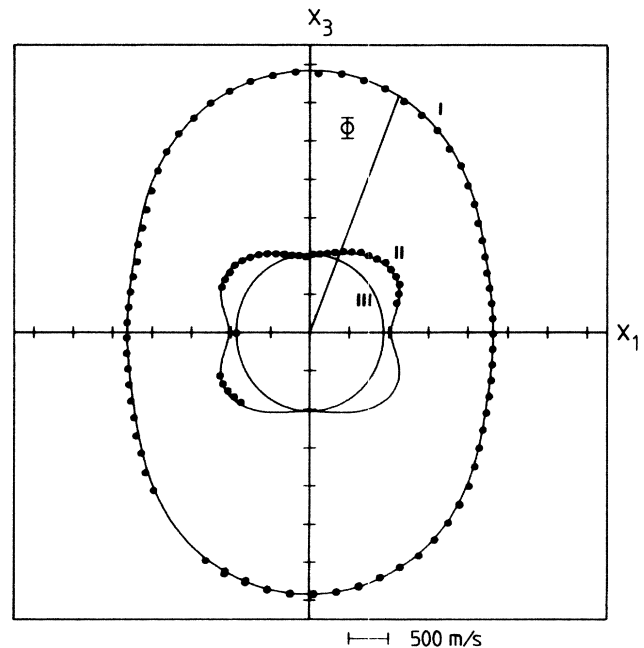


FIG. 4. Sound velocity polar plot of sample A for \mathbf{q} oriented in the (x_1, x_3) plane, measured at room temperature. Curve I, sound velocities of QL sound waves; curve II, sound velocities of quasitransverse sound waves; curve III, sound velocity of the pure shear mode. $\Phi = \angle(\mathbf{q}, x_3)$.

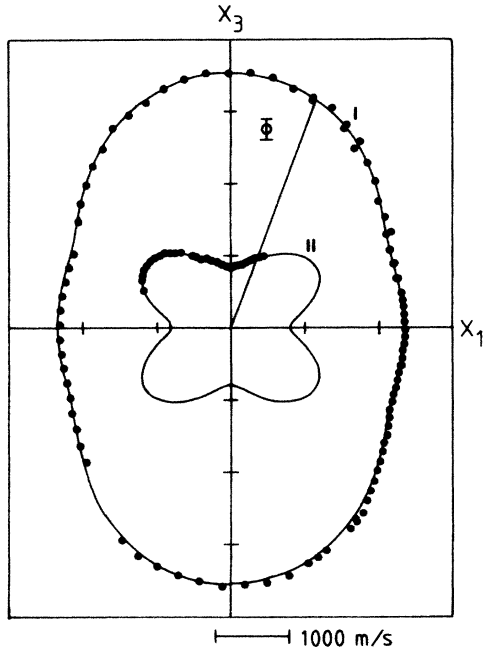


FIG. 5. Sound velocity polar plot of sample B of \mathbf{q} oriented in the (x_1, x_3) plane, measured at room temperature. Curve I, sound velocities of QL sound waves; curve II, sound velocities of quasitransverse sound waves. $\Phi = \angle(\mathbf{q}, \mathbf{x}_3)$.

measurements using the fact that for sound propagation along the x_3 axis the quasitransverse and the transverse mode degenerate yielding $v = \sqrt{c_{44}/\rho}$. The point on the x_1 axis results from 90R measurements along the equivalent x_2 axis with the incident laser light polarized along the x_1 axis (orthogonal to the scattering plane) and the scattered light polarized within the scattering plane (VH polarization) yielding $v = \sqrt{c_{66}/\rho}$. Because of the small scattering cross section and the bad optical properties of the smectic sample B, 90R measurements were not yet successful. The stiffness coefficient c_{66} for this material and the related curve III in Fig. 5 are therefore missing.

The basic relation for the determination of the elastic stiffness coefficients from the measured data is the Christoffel equation. Assuming fiber symmetry for the monodomain samples, this leads to the following cubic eigenvalue equation:

$$\det[\mathbf{IcI}^T - \mathbf{E}c_{\hat{\mathbf{q}}}] = 0, \quad (1)$$

with

$$\mathbf{I} = \begin{pmatrix} I_1 & 0 & 0 & 0 & I_3 & I_2 \\ 0 & I_2 & 0 & I_3 & 0 & I_1 \\ 0 & 0 & I_3 & I_2 & I_1 & 0 \end{pmatrix}, \quad (2)$$

$$\mathbf{c} = \mathbf{c}^T = \begin{pmatrix} c_{11} & c_{12} & c_{13} & 0 & 0 & 0 \\ c_{12} & c_{11} & c_{13} & 0 & 0 & 0 \\ c_{13} & c_{13} & c_{33} & 0 & 0 & 0 \\ 0 & 0 & 0 & c_{44} & 0 & 0 \\ 0 & 0 & 0 & 0 & c_{44} & 0 \\ 0 & 0 & 0 & 0 & 0 & c_{66} \end{pmatrix}, \quad (3)$$

$$c_{\hat{\mathbf{q}}} = \rho\omega^2/q^2 = \rho v^2,$$

and

$$\hat{\mathbf{q}} = (I_1, I_2, I_3) = I_1 \mathbf{x}_1 + I_2 \mathbf{x}_2 + I_3 \mathbf{x}_3. \quad (4)$$

\mathbf{x}_i ($i=1,2,3$) are the unit vectors in the coordinate directions of the sample coordinate system, $\mathbf{q} = q\hat{\mathbf{q}}$ is the acoustic wave vector, I_i ($i=1,2,3$) are the direction cosines of \mathbf{q} , c_{ij} ($i, j=1,2, \dots, 6$) are the elastic stiffness coefficients (Voigt notation), $f = \omega/2\pi$ is the sound frequency, v is the sound velocity, ρ is the mass density, $c_{\hat{\mathbf{q}}}$ are eigenvalues which have been measured by Brillouin spectroscopy for different directions $\hat{\mathbf{q}}$ of phonon propagation, and \mathbf{E} is the unit matrix. An appropriate data analysis procedure using Eqs. (1)–(4) and Marquardt's nonlinear least-squares fit combined with the formula of Cardano^{10(b)} yields for sample A the complete elastic stiffness tensor, whereas for sample B the shear coefficient c_{66} is missing. The results including the compliance tensor $\{s_{ij}\}$ of sample A are given in Table II.

With the exception of the shear coefficient c_{44} , the nematic and the smectic, samples A and B, respectively, exhibit an almost identical elastic behavior. Both show a strong elastic anisotropy, comparable to that found in mechanically oriented amorphous polymers.²¹ The coefficients c_{33} are at room temperature more than twice as large as c_{11} , indicating a pronounced increase of the longitudinal elastic stiffness along the preferential orientation of the mesogenic side chains. The influence of the preferential orientation of the backbone molecules (orthogonal to the director) on the elastic properties are overcompensated by the ordering of the mesogenic side chains. Our earlier results on a PLC containing chromophore molecules^{10(b)} are therefore at least qualitatively confirmed.

The difference in the elastic characteristics of monodomain CLC's on the one hand, and of monodomain

TABLE II. Elastic stiffness coefficients c_{ij} (GPa) of samples A and B and the compliance coefficients s_{ij} (GPa⁻¹) of sample A at room temperature. The given deviations Δc_{ij} hold for both samples.

	c_{33}	c_{11}	c_{44}	c_{66}	c_{13}	s_{33}	s_{11}	s_{44}	s_{66}	s_{13}
Sample A	12.86	5.90	1.15	0.95	4.76	0.12	0.34	0.87	1.05	-0.06
Sample B	12.50	5.49	0.64		4.00					
$\pm \Delta c_{ij}$	0.02	0.03	0.02	0.05	0.03					

PLC's on the other hand, can be understood as follows. Monodomain CLC's deform under stress primarily by translation of the nearly rigid molecules relative to each other. This shift strains mainly van der Waals bonds. Apparently these displacements take place with similar ease parallel and perpendicular (depending on the applied stress) to the axis of the director (x_3 axis). Such systems therefore behave almost elastically isotropic.

In PLC's, on the other hand, the translations of the mesogenic side groups relative to each other are hindered by the coherency of these groups via the polymer backbone. This restraining influence is more pronounced for deformations parallel to the preferred side chain orientation than for deformations perpendicular to it. This is understandable, since the former require either (i) a straining of the relatively rigid side chains, (ii) a strong local deformation of the polymer backbone, or (iii) an orientational change of the mesogenic groups involving straining of covalent and polar bonds. The latter, on the other hand, require only smooth deformations of the backbone in addition to changes in the van der Waals interactions. This difference explains qualitatively the observed elastic anisotropy.

Only a small difference is observed between the shear stiffnesses c_{44} and c_{66} for the nematic sample A. c_{44} and c_{66} are comparable to those found in (oriented) amorphous polymers^{19,22,23} and oligomers.^{10(a)} The remarkable size of these values is a consequence of the frequency-dependent imaginary part of the complex shear viscosity, which leads to a real elastic shear constant at high frequencies ($\omega\tau \gg 1$, where τ is the relaxation time of the corresponding shear viscosity). It is obvious that neither $[c_{44}]^{-1}$ nor $[c_{66}]^{-1}$ diverge in the nematic state.

For the nematic sample A sound velocity polar plots have been determined with increasing temperature up to the isotropic state. Using the procedure described above we could calculate the stiffness coefficients c_{11} , c_{33} , c_{44} , c_{66} , and c_{13} as functions of temperature (●, Fig. 6). On slow cooling through T_{ni} the same monodomain state could be reproduced (○, Fig. 6).

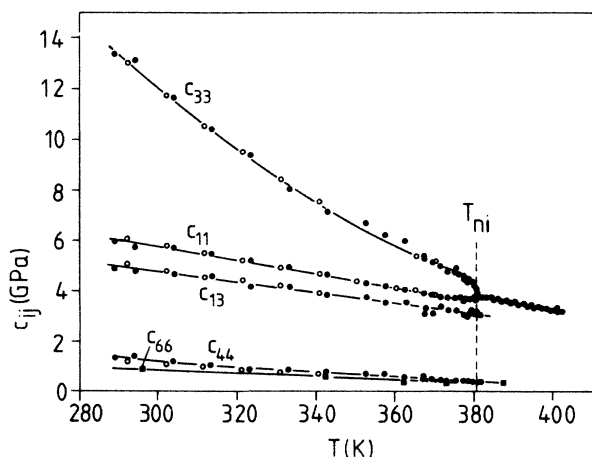


FIG. 6. Elastic stiffness coefficients c_{ij} of the nematic sample A as functions of temperature T . T_{ni} , transition temperature at the nematic-isotropic transition (●, with increasing temperature; ○, with decreasing temperature).

The strongest influence of the order parameter is reflected by the temperature behavior of the coefficient c_{33} . The other coefficients are only slightly affected. As expected, the behavior of c_{11} in the nematic phase is comparable to the behavior of c_{11}^{iso} (in the isotropic phase) if the latter is extrapolated to the nematic phase.

Although the nematic-isotropic transition is weakly of first order (Svetkov-order parameter $S \approx 0.25$), the elastic stiffness coefficients and the refractive indices n_i (Fig. 8) behave continuously at T_{ni} (within the error limits). This may be partly due to a rather broad distribution of the molecular weights of the polymer chains which leads to a smearing out of the transition. From the elastic properties it follows, therefore, that the transition may be described approximately as a second-order transition (Fig. 6) with a coupling between the static order parameter and the elastic strain component ϵ_{33} . Qualitatively the temperature dependence of c_{33} for $T < T_{ni}$ suggests a quadratic coupling between the order parameter and the elastic strain ϵ_{33} described by a free-energy density term $F_c = \delta S \epsilon_{33}^2$, where δ is a constant.²⁴ Unfortunately the behavior of the elastic stiffness constants with temperature results from a superposition of the nematic-isotropic transition and the glass transition, whose relative contributions to the elastic anomalies cannot yet be determined. The quasistatic glass transition of sample A occurs at $T_g = 295$ K (Table I). The dynamic glass transition is therefore expected to develop above room temperature and to interfere with the LC transition.

A clear indication for the influence of the dynamic glass transition on the elastic properties is the temperature dependence of special optoacoustic functions, which we call D functions.^{10(a),10(b)} For the following discussion we define only those, from which, in the absence of hypersonic dispersion, the refractive indices n_i ($i=1,3$) of our samples can be deduced. Assuming $c'' \ll c'$ one has

$$D_i^{90R}(\hat{q}) = \{ [c'^{90R}(\hat{q}, \mathbf{p}) / c'^{90A}(\hat{q}, \mathbf{p})] (n_i^2 - 0.5) + 0.5 \}^{1/2}. \quad (5)$$

c' and c'' are the real and imaginary parts of the complex elastic stiffness modulus $c^* = c' - jc''$. \mathbf{p} gives the polarization of the sound mode involved.

Keeping in mind that \mathbf{x}_1 and \mathbf{x}_2 define symmetry equivalent directions, the D_i^{90R} functions can be evaluated from easily measurable sound frequencies using the following scattering conditions. (i) 90A-scattering geometry: \mathbf{q} parallel to \mathbf{x}_1 and the electric field vectors \mathbf{E}_{inc} and \mathbf{E}_{sc} of the incident and scattered laser light parallel to \mathbf{x}_3 . The wavelength Λ^{90A} of the longitudinal sound mode along \mathbf{x}_1 is then independent of the optical properties,

$$\Lambda^{90A} = \lambda_0 / \sqrt{2}. \quad (6)$$

(ii) 90R-scattering geometry: \mathbf{q} parallel to \mathbf{x}_2 and \mathbf{E}_{inc} and \mathbf{E}_{sc} both parallel to \mathbf{x}_i ($i=1,3$). The wavelength Λ^{90R} of the longitudinal sound mode involved in the 90R-

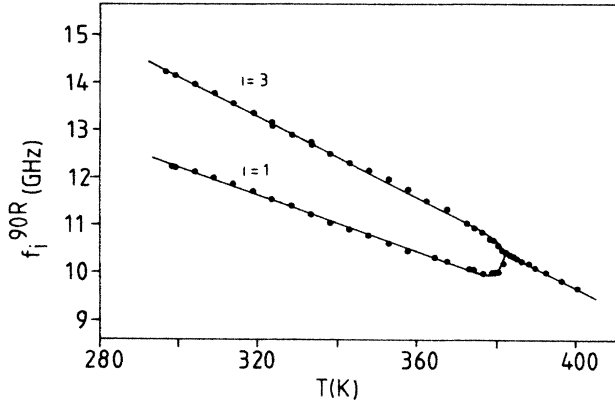


FIG. 7. Sound frequencies of the longitudinal polarized acoustic modes of sample A as a function of temperature for propagation along \mathbf{x}_2 , using the 90R-scattering geometry. The electric field vectors are chosen to be $\mathbf{E}_i \parallel \mathbf{E}_s \parallel \mathbf{x}_1$ and $\parallel \mathbf{x}_3$, respectively.

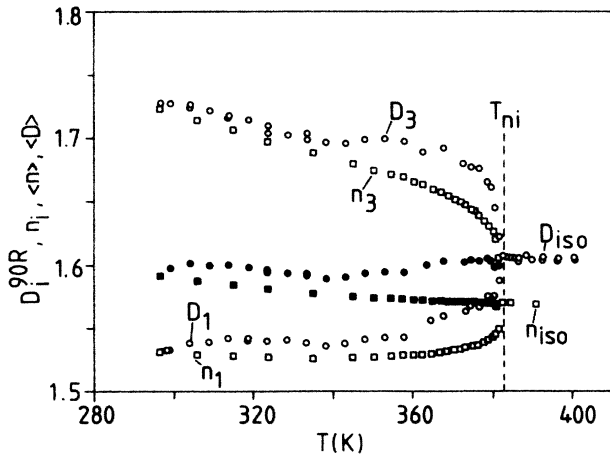


FIG. 8. D_i^{90R} and n_i ($i=1,3$) of sample A as a function of temperature T . n_{iso} , refractive index of the isotropic state; D_{iso} , D^{90R} function of the isotropic state; \bullet , $\langle D \rangle$; \blacksquare , $\langle n \rangle$.

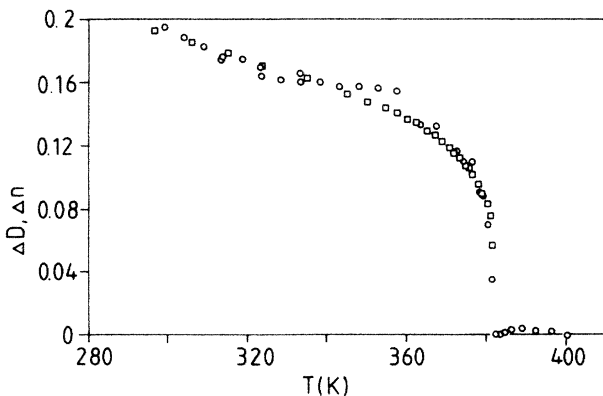


FIG. 9. ΔD and Δn as a function of temperature T of the nematic sample A. \square , Δn ; \circ , ΔD .

scattering experiment depends on n_i ,

$$\Lambda^{90R} = \lambda_0 / [(4n_i^2 - 2)]^{1/2}, \quad (i=1,3). \quad (7)$$

From Eqs. (5)–(7) we get the desired relation between D_i^{90R} and the measured frequencies,

$$D_i^{90R}(\mathbf{x}_{\hat{q}}) = (\{ [f_i^{90R}(\mathbf{x}_2) / f^{90A}(\mathbf{x}_1)]^2 + 1 \} / 2)^{1/2}, \quad i=1,3. \quad (8)$$

$\mathbf{x}_{\hat{q}}$ represents the set of symmetry equivalent directions of type \mathbf{x}_i . As mentioned in Sec. II, we can measure the hypersonic frequencies $f_i^{90R}(\mathbf{q} \parallel \mathbf{x}_2)$ and $f^{90A}(\mathbf{q} \parallel \mathbf{x}_1)$ simultaneously from the same scattering volume (cf. Fig. 1). If hypersonic dispersion is negligible this experimental procedure yields the refractive indices $n_1 = n_2$ and n_3 besides the elastic stiffness modulus $c_{11} = c_{22}$. Making use of the optical analyser PO (Fig. 1) to realize the scattering conditions for the detection of transverse phonons the stiffness coefficients c_{44} and c_{66} can be obtained, at least in principle.

The quantity $(D_i^{90R} - n_i)$ is a sensitive indicator for hypersonic dispersion. For normal dispersion, $(D_i^{90R} - n_i) \geq 0$ holds. This probe for acoustic dispersion effects is of special interest if the phonon line widths are difficult to obtain, as in the case of the present measurements on thin liquid crystal film. Even if n_i is not precisely known, the temperature dependence of the D functions can be used as an indicator for the presence of sound dispersion in the hypersonic region.

Figure 7 shows the temperature dependences of the sound frequencies f_i^{90R} ($i=1,3$). At any temperature the difference between these frequencies is mainly due to the difference of the refractive indices n_1 and n_3 .

Equation (8) has been used to determine D_i^{90R} ($i=1,3$) for sample A. Figure 8 shows $D_1^{90R}(T)$ and $D_3^{90R}(T)$ in comparison with $n_1(T)$ and $n_3(T)$. Above room temperature the deviation of the D^{90R} functions from the corresponding n functions increases with temperature, indicating the onset of an acoustic relaxation process at hypersonic frequencies. Since the increase becomes even stronger in the isotropic state, this relaxation process can be attributed to a glass relaxation process.^{10(a), 10(b), 22} In contrast to our earlier results on a different (polydomain) PLC (Ref. 9) there is no hint of order-parameter fluctuations at hypersonic frequencies in the vicinity of the nematic-isotropic transition. In addition to the n_i and D_i^{90R} values we present the orientation-averaged data $\langle n \rangle = (2n_1 + n_3)/3$ (\blacksquare , Fig. 8) and $\langle D^{90R} \rangle = (2D_1^{90R} + D_3^{90R})/3$ (\bullet , Fig. 8) for the nematic phase of sample A. Both quantities show no anomalies at T_{ni} .

Finally the n functions have been used to calculate the birefringence $\Delta n = n_3 - n_1$ as a measure for the static order parameter (Fig. 9). As expected, only small deviations appear between Δn (\square , Fig. 9) and $\Delta D = D_3^{90R} - D_1^{90R}$ (\circ , Fig. 9), indicating that in contrast to the D^{90R} functions themselves, the $\Delta D(T)$ function (determined only from Brillouin data) is also a good measure for the static order parameter.

- ¹(a) H. Kelker and R. Hatz, *Handbook of Liquid Crystals* (Verlag Chemie, Weinheim, 1980); (b) P. G. de Gennes, *The Physics of Liquid Crystals* (Clarendon, Oxford, 1979); (c) S. Chandrasekhar, *Liquid Crystals* (Cambridge Monographs on Physics, Cambridge, 1980).
- ²K. Miyano and J. B. Ketterson, in *Physical Acoustics*, edited by W. P. Mason (Academic, New York, 1979), Vol. XIV, p. 93ff.
- ³A. Wergin, W. Krasser, H. H. Stiller, and C. G. B. Frischkorn, *Phys. Rev. A* **20**, 1120 (1979).
- ⁴M. Copic, M. Zgonik, and B. B. Lavrencic, *J. Phys. Lett.* **42**, L405 (1981).
- ⁵Y. Liao, N. A. Clark, and P. S. Pershan, *Phys. Rev. Lett.* **30**, 639 (1973).
- ⁶G. R. Strobl, *Colloid Polym. Sci.* **254**, 170 (1976).
- ⁷J. K. Krüger, M. Pietralla, and H.-G. Unruh, *Phys. Status Solidi A* **71**, 493 (1982).
- ⁸A. Marx and J. K. Krüger (to be published).
- ⁹J. K. Krüger, L. Peetz, R. Zentel, and P. Claudy, *Phys. Lett.* **114A**, 51 (1986).
- ¹⁰J. K. Krüger, A. Marx, R. Roberts, H.-G. Unruh, M. B. Bitar, H. Nguyen-Trong, and H. Seliger, *Makromol. Chem.* **185**, 1469 (1984); (b) J. K. Krüger, A. Marx, L. Peetz, R. Roberts, and H.-G. Unruh, *Colloid Polym. Sci.* **264**, 403 (1986).
- ¹¹H. Hirschmann, masters thesis, Technische Hochschule Darmstadt, 1987.
- ¹²R. G. Kirste and H. G. Ohm, *Makromol. Chem., Rapid Commun.* **6**, 179 (1985).
- ¹³P. Keller, B. Carvalho, J. P. Cotton, M. Lambert, F. Moussa, and G. Pepy, *J. Phys. Lett.* **46**, L1065 (1985).
- ¹⁴A. B. Kunchenko and D. A. Svetogorski, *J. Phys.* **47**, 2015 (1986).
- ¹⁵H. Finkelmann, and G. Rehage, *Adv. Polym. Sci.* **60-61**, 99 (1984).
- ¹⁶M. Wolf, and J. H. Wendorff, *Mol. Cryst. Liq. Cryst.* **149**, 141 (1987).
- ¹⁷J. K. Krüger, R. Kimmich, J. Sandercock, and H.-G. Unruh, *Polym. Bull.* **5**, 615 (1981).
- ¹⁸J. K. Krüger, L. Peetz, and M. Pietralla, *Polymer* **19**, 1397 (1978).
- ¹⁹J. K. Krüger, L. Peetz, W. Wildner and M. Pietralla, *Polymer* **21**, 620 (1980).
- ²⁰B. A. Auld, *Physical Acoustics* (Wiley, New York, 1973), Vol. I.
- ²¹I. M. Ward, *Developments in Oriented Polymers-1* (Applied Science Publishers, London, 1982).
- ²²J. K. Krüger, R. Roberts, H.-G. Unruh, K. P. Frühauf, J. Helwig, and H. E. Müser, *Prog. Colloid Polym. Sci.* **71**, 77 (1985).
- ²³L. Peetz, J. K. Krüger, and M. Pietralla, *Colloid Polym. Sci.* **265**, 761 (1987).
- ²⁴W. Rehwald, *Adv. Phys.* **22**, 721 (1973).